AGU PUBLICATIONS

JGR

Journal of Geophysical Research: Atmospheres

RESEARCH ARTICLE
10.1002/2014JD022138

Key Points:

- Column fine mode AOD greatly exceeds expected values from surface measurements
- Coarse mode AOD is confined to the convective boundary layer
- Coarse mode aerosol depletes fine mode aerosol by coagulation and condensation

Correspondence to:
S. M. Loría-Salazar,
marce.marcelaloria@gmail.com

Citation:
Loría-Salazar, S. M., W. P. Arnott, and H. Moosmüller (2014), Accuracy of near-surface aerosol extinction determined from columnar aerosol optical depth measurements in Reno, NV, USA, *J. Geophys. Res. Atmos.*, *119*, doi:10.1002/2014JD022138.

Received 4 JUN 2014
Accepted 24 AUG 2014
Accepted article online 28 AUG 2014

Accuracy of near-surface aerosol extinction determined from columnar aerosol optical depth measurements in Reno, NV, USA

S. Marcela Loría-Salazar[1], W. Patrick Arnott[2], and Hans Moosmüller[1]

[1]Division of Atmospheric Sciences, Desert Research Institute, Reno, Nevada, USA, [2]Department of Physics and Atmospheric Sciences, University of Nevada, Reno, Nevada, USA

Abstract The aim of the present work is a detailed analysis of aerosol columnar optical depth as a tool to determine near-surface aerosol extinction in Reno, Nevada, USA, during the summer of 2012. Ground and columnar aerosol optical properties were obtained by use of in situ Photoacoustic and Integrated Nephelometer and Cimel CE-318 Sun photometer instruments, respectively. Both techniques showed that seasonal weather changes and fire plumes had enormous influence on local aerosol optics. The apparent optical height followed the shape but not magnitude of the development of the convective boundary layer when fire conditions were not present. Back trajectory analysis demonstrated that a local flow known as the Washoe Zephyr circulation often induced aerosol transport from Northern California over the Sierra Nevada Mountains that increased the aerosol optical depth at 500 nm during afternoons when compared with mornings. Aerosol fine mode fraction indicated that afternoon aerosols in June and July and fire plumes in August were dominated by submicron particles, suggesting upwind urban plume biogenically enhanced evolution toward substantial secondary aerosol formation. This fine particle optical depth was inferred to be beyond the surface, thereby complicating use of remote sensing measurements for near-ground aerosol extinction measurements. It is likely that coarse mode depletes fine mode aerosol near the surface by coagulation and condensation of precursor gases.

1. Introduction

Aerosols and greenhouse gases are forcing agents of the atmospheric radiation budget. The influence of greenhouse gases (aerosols) on the radiative forcing is well (poorly) understood. Depending on their nature and that of the underlying scene, aerosols have the ability to warm (through light absorption) or cool (through light scattering) the atmosphere: they alter the surface energy budget [*Chylek and Wong*, 1995]. Unfortunately, even today, a lack of knowledge and observations hinder answering key questions about the role of aerosols in climate change [*Solomon et al.*, 2007; *Stocker et al.*, 2013]. Aerosols also are linked with air pollution [*Finlayson-Pitts and Pitts*, 1997], visibility impairment [*Watson*, 2002], and health problems [*Pope and Dockery*, 2006]. In addition, a substantial aerosol fraction also acts as cloud condensation nuclei, thereby affecting cloud reflectivity [*Twomey*, 1977; *Lensky and Rosenfeld*, 1998].

Primary aerosols are directly emitted from their sources into the ambient atmosphere. Secondary aerosols are formed in atmospheric chemical and photochemical reactions among particles, gases, and sunlight. In order to improve temporal and global monitoring of aerosol pollution, satellite remote sensing and ground-based Sun photometry were established; these technologies have been extensively developed since the 1990s [*Holben et al.*, 1996]. Satellite remote sensing offers broad temporal and spatial coverage for global aerosol pollution monitoring. Ground-based Sun photometry provides highly accurate column aerosol optical depth (τ_{ext}) measurements for evaluating satellite retrievals and characterizing local conditions [*Remer et al.*, 2005].

Reno, Nevada, USA, is a midsize town located in a valley where ambient air often contains typical urban aerosols, wind-blown mineral dust, and biomass burning emissions from natural and prescribed fires. The Sierra Nevada Mountains complicate air pollution transport from California due to the interaction with biogenic emissions [*Hoffmann et al.*, 1997; *Griffin et al.*, 1999a, 1999b], sunlight, and flow over complex terrain.

The vertical profile of aerosol in the atmosphere has been much less studied than horizontal variability because of the added challenge in sampling the atmosphere aloft [*Andrews et al.*, 2011]. Passive ground-based and satellite retrievals of aerosol optical depth and microphysics are based on assumptions about vertical aerosol profiles, sometimes leading to errors [*Rozwadowska*, 2007]. Previous research on aerosol vertical profile was performed at the Southern Great Plains (SGP) Atmospheric Radiation Measurement site in Oklahoma from April 1996 to March 1997. The main challenge in one of their methods to retrieve τ_{ext} was due to the assumption that aerosol was present in a well-mixed boundary layer without any contribution to aerosol extinction from above. They concluded that at the SGP site, it was not possible to use surface measurements alone to specify column aerosol optical depth [*Bergin et al.*, 2000]. One purpose of this paper is to provide a simple methodology for analysis of whether aerosol resides in a well-mixed state, mostly in the atmospheric convective boundary layer or not.

Previous research looked at the relationship between column aerosol optical depth and surface extinction coefficients reconstructed from chemical measurements in urban Washington, D.C. [*Corbin et al.*, 2002]. They found a modest correlation for data averaged into biweekly samples to match the schedule of chemical analysis. They hypothesized that the vertical distribution of aerosol mass, composition, and relative humidity were not the same as at the surface, thereby affecting the relationship of the surface extinction coefficient and column aerosol optical depth (AOD). Our study is similar to theirs, although we make use of direct measurements of aerosol extinction coefficient and its scattering and absorption components, and we look at the diurnal trends by using 1 h time averages during daylight hours. Later work presented favorable comparisons of aerosol fine mode properties retrieved from in situ cavity ringdown extinction measurements and Aerosol Robotic Network (AERONET) values, although there were no column versus surface comparisons of aerosol optical depth derived from boundary layer height and Sun photometer [*Atkinson et al.*, 2010].

The eventual goal of our research is to use satellite remote sensing of column τ_{ext} for determining surface relevant aerosol information, such as $PM_{2.5}$ mass concentration [*Hoff and Christopher*, 2009] near the surface. A prerequisite for the satellite study is a detailed analysis, reported here for our mountainous western U.S. location, of the comparison of column τ_{ext} from highly accurate Sun photometers with in situ photoacoustic and reciprocal nephelometer instruments that measure the directly comparable spectrally resolved in situ ground-level aerosol extinction coefficients (denoted by the symbol β_{ext}). This approach is in lieu of establishing a relationship between $PM_{2.5}$ mass concentration and aerosol optical properties.

2. Instruments and Data

Aerosol light absorption coefficients were measured with a dual wavelength photoacoustic instrument [*Lewis et al.*, 2008]. The Photoacoustic and Integrated Nephelometer (PIN) spectral channels used in the experiment were 405 and 870 nm. Observations with the photoacoustic instrument are based on use of a power-modulated laser beam that induces periodic particle temperature change due to light absorption, followed by air temperature variation due to heat transfer. The instrument quantifies the generated acoustic pressure of the surrounding air at the laser modulation frequency yielding the absorption coefficient [*Arnott et al.*, 1999, 2000]. A reciprocal integrating nephelometer using the same sample volume utilizes an optical detector that measures the scattering coefficient [*Lewis et al.*, 2008]. The scattering and absorption measurements have 15% and 5% relative uncertainty, respectively. The error bars and smoothing algorithm used for the PIN measurements are discussed further in Appendix A.

Cimel CE-318 Sun photometer measures direct solar and sky irradiance and quantifies aerosol optical properties for the entire atmospheric column. The wavelengths used in this study were 440, 500, and 870 nm where gaseous absorption is manageable. Cimel provides very accurate and precise measurements of atmospheric column optics [*Holben et al.*, 1998]. Cimel CE-318 is the standard instrument used in the Aerosol Robotic Network (AERONET). AERONET retrieves aerosol optical properties through cloud-screened, direct Sun, and almucantar scans [*Holben et al.*, 1998].

AERONET's algorithms were initially based on the assumption of spherical particle shape [*Dubovik and King*, 2000]. The *Dubovik et al.* [2006] version was developed for more general nonspherical particles to improve retrievals in desert areas. Aerosol optical depth is measured by direct Sun observations during all daylight hours. Retrievals related to sky scans are limited to certain daylight hours [*Dubovik et al.*, 2002]. The first limitation is that the solar zenith angle must be larger than 50°, which prevents retrieval of the aerosol size distribution close to local midday at low-latitude locations [*Dubovik et al.*, 2000]. The second issue is that the single scattering albedo (SSA) uncertainty is very high if the τ_{ext} at 440 nm is smaller than 0.4 [*Dubovik et al.*, 2002] so that typical conditions in Reno are often not conducive to SSA retrieval.

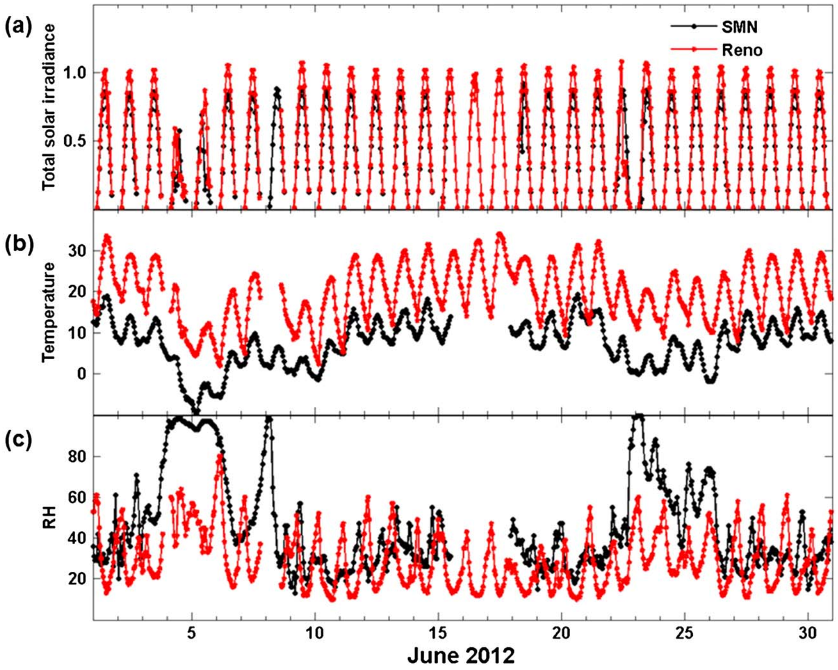

Figure 1. Hourly average of meteorological conditions measured at Slide Mountain, Nevada and Reno, weather stations in June 2012. (a) Total solar irradiance (arbitrary units). (b) Temperature (°C). (c) Relative humidity (%).

For this study, temperature, relative humidity, solar irradiance, as well as wind speed and direction were obtained from Slide Mountain Nevada (SMN) and the University of Nevada, Reno, (UNR) weather stations in order to link the atmospheric aerosol conditions with weather variables (Figures 1–3). The SMN weather station is located at 39.3° latitude north and 119.8° longitude west with an elevation of 2.9 km, and the UNR weather station is located at 39.5° latitude north and 119.8° longitude west with an elevation of 1.4 km.

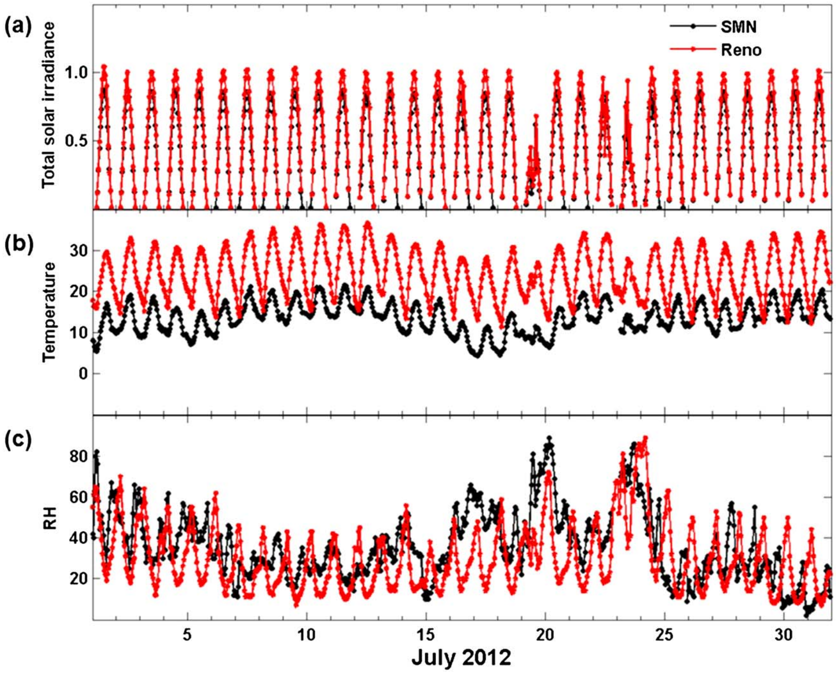

Figure 2. Same as Figure 1 but for July 2012.

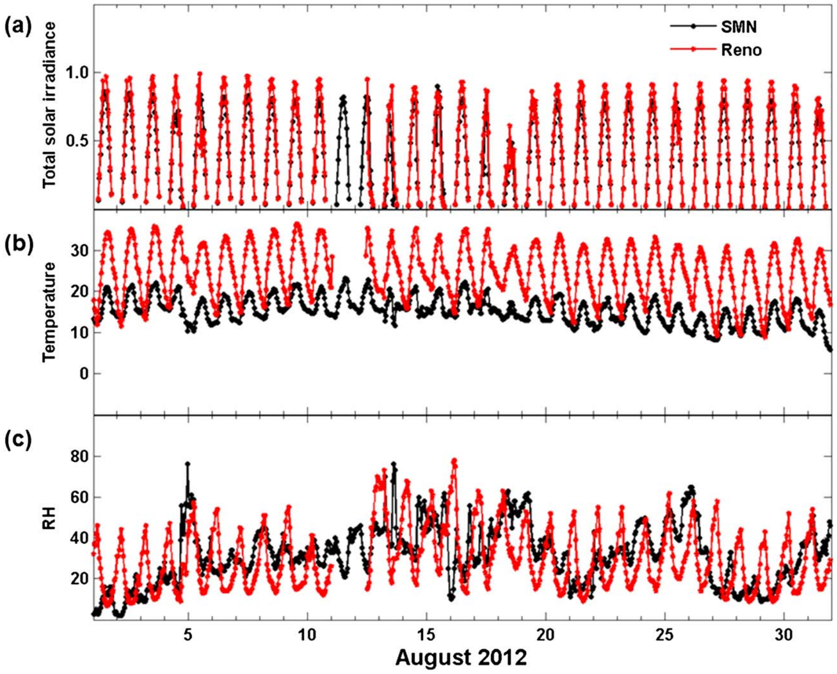

Figure 3. Same as Figure 1 but for August 2012.

Relative humidity (RH) from atmospheric balloon soundings by the Reno-National Weather Service was used in order to investigate possible aerosol hygroscopic growth of τ_{ext} in the vertical due to very high RH [*Remer et al.*, 1998]. Vertical dew point temperature diminishment and vertical potential temperature inversion methods from balloon soundings aimed to retrieve the average height of the convective boundary layer (CBL) at 5 P.M. In addition, wind speed and direction were used to study local circulation and its relationship to aerosol transport and cleaning mechanisms. Finally, back and forward trajectory analysis with the HySplit model [*Draxler and Rolph*, 2013; *Rolph*, 2013] was used to study aerosol transport phenomena.

3. Methodology

Columnar and surface-level measurements of atmospheric aerosol optical properties were performed using Cimel CE-318 and PIN, respectively, for June, July, and August 2012. Additionally, local weather observations from multiple weather stations, Reno balloon soundings, and back trajectory analyses were added to understand the role of local weather conditions on aerosol formation, growth, and transport.

This work is based on the University of Nevada, Reno, AERONET station Level 1 (manually screened for cloud contamination) in order to detect the sometimes highly variable fire plumes in August that would otherwise be classified as clouds. June and July AOD and coarse mode fraction data were from the Level 1.5 collection (real-time cloud-screened data), and Level 2 (cloud-screened and quality-assured data) was used for the size distribution data reported in Appendix B. The site is located at 39.54° latitude north and 119.84° longitude west; τ_{ext} uncertainty is estimated to be in the range of ~0.01 to ~0.05 (air mass equals 1) [*Eck*, 2010]. The instrument collimator was checked weekly in order to ensure that the data were not corrupted by contaminants, such as dust deposits on optical windows. Days with less than three valid measurement points were not used.

The observation period was from 1 June to 31 August 2012, with predominance of dry conditions and high temperatures. Figures 1a, 2a, and 3a show total solar irradiance during the study months. Solar irradiance profiles allowed us to identify the cloud-impacted days—4, 5, 15, 16, 22, and 23 June, 19, 27, and 28 July, and 18 August—which were eliminated from analysis in order to ensure the accuracy of aerosol data from the Cimel CE-318.

Temperature time series from UNR and SMN weather stations are displayed in Figures 1b, 2b, and 3b. June presented a mix of low and high temperatures characteristic of a transition month. July and August temperatures were consistently higher than those in June. Relative humidity (RH) in Figures 1c, 2c, and 3c was lower than 65%, except for the cloud-contaminated days for which data were not analyzed. These low-RH conditions allowed for analysis of aerosol optical properties without accounting for hygroscopic growth [*Sheridan et al.*, 2002; *Andrews et al.*, 2004].

In addition, columnar RH from balloon soundings presented in Figure 4 generally agreed with surface measurements. August presented high values of RH in the column for days affected by California forest fires. Figure 5a shows a Terra/Moderate Resolution Imaging Spectroradiometer (MODIS) satellite image of the study area containing an example of a regional fire burning close to Lake Almanor, California. Most of the area burned by this fire was covered with pine forest. *Lewis et al.* [2009] found that particles formed by pine litter fires do not exhibit strong hygroscopic growth.

4. Analysis

4.1. Daily Aerosol Optics and Weather Relationships

Aerosol optical depth (τ_{ext}) is the path-integrated sum of aerosol light scattering and absorption coefficients. Atmospheric aerosols are carried away from their sources by the wind and are subject to chemical and physical modifications when exposed to meteorological variables such as temperature, relative humidity, and total solar irradiance as well as to biogenic emissions from forests. The Ångström Extinction Exponent (AEE) is related to the Ångström Scattering Exponent and the Ångström Absorption Exponent [*Moosmüller and Chakrabarty*, 2011] and describes the dependence of τ_{ext} on wavelength [*Schuster et al.*, 2006; *Kaskaoutis et al.*, 2007]. AEE is a qualitative indicator of particle size [*Ångström*, 1929; *Eck et al.*, 1999]. AEE is inversely related to the size of the particle; the larger the AEE, the smaller the particle. Typically, coarse mode aerosols such as dust and sea salt have values of AEE ~1. AEE $\geq$ 2 designates size distributions dominated by fine mode aerosols related to biomass burning and urban pollution [*Eck et al.*, 1999]. Most atmospheric aerosols have AEE in the range between 1 and 2 [*Prats et al.*, 2011] for the wavelength range of this study.

Figures 5b and 5c show observations from AERONET (440 nm) and 30 min averages from PIN (405 nm) made on 3 August 2012 that demonstrate the increase of τ_{ext} and extinction coefficient, respectively, due to the fire impact. The maximum in τ_{ext} (Figure 5b) observed between 10 and 11 A.M. did not correspond to a similar maximum for the near-surface extinction coefficient (Figure 5c). The τ_{ext} started to diminish at 1 P.M. as did the near-surface extinction, but a secondary maximum in τ_{ext} was observed between 1 P.M. and 3 P.M. that did not appear in the near-surface extinction measurements. This is one example of a fire plume that had a complicated vertical structure so that column τ_{ext} did not always reflect surface conditions.

Figures 6a, 7a, and 8a display daily τ_{ext} distribution at 500 nm during the summer months; τ_{ext} values show June as a month with low aerosol pollution (Figure 6a). The maximum value of τ_{ext} was 0.15. The gaps between days represent the presence of clouds typical during the transition of seasons. Previous in situ studies in Reno [*Gyawali et al.*, 2009] showed that aerosol light extinction coefficients for nonfire conditions peaked during the morning rush hour (from 6 A.M. to 11 A.M.) and stabilized nearly symmetrically and with low values on either side of the maximum. However, τ_{ext} for some representative June days kept increasing during the day. In particular, τ_{ext} on 1, 14, and 27 June, highlighted in yellow, kept increasing until the late afternoon, as will be discussed further below.

Overall, τ_{ext} values in July were slightly higher than those in June (Figures 6a and 7a). Aerosol optics on 2 July was affected by a fire plume (Figure 7). The maximum τ_{ext} value during this event was 0.37; 8, 14, and 26 July presented the prolonged daily increase in τ_{ext} that was also observed in June (1, 14, and 27), highlighted in yellow. August τ_{ext} (Figure 8a) was influenced by California forest fires (Figures 5a–5c). Most of the time, τ_{ext} values were higher than those observed during the previous 2 months. The maximum value of τ_{ext} for August was 0.72. The prolonged increase in daily τ_{ext} was not observed during August.

A relationship between temperature and aerosol pollution on the west side of the Sierra Nevada Mountains (SNM) was studied during the Carbonaceous Aerosols and Radiative Effects Study (CARES) field campaign in 2010. According to *Zaveri et al.* [2012], levels of aerosol pollution were highest during warmer temperatures and the end of the period (25–28 June 2010). Our east side study of SNM reported similar results. June 2012 exhibited lower values of temperature and τ_{ext} compared to later months; τ_{ext} increased as the temperature became warmer in July and August, likely causing enhancement of secondary organic aerosol formation. The evolution of AEE is shown in Figures 6b, 7b, and 8b (diurnal variation plots are presented in section 4.3 to provide more detail). In general, AEE anticorrelated with τ_{ext} on most of the nonsmoky days. It is likely that fine

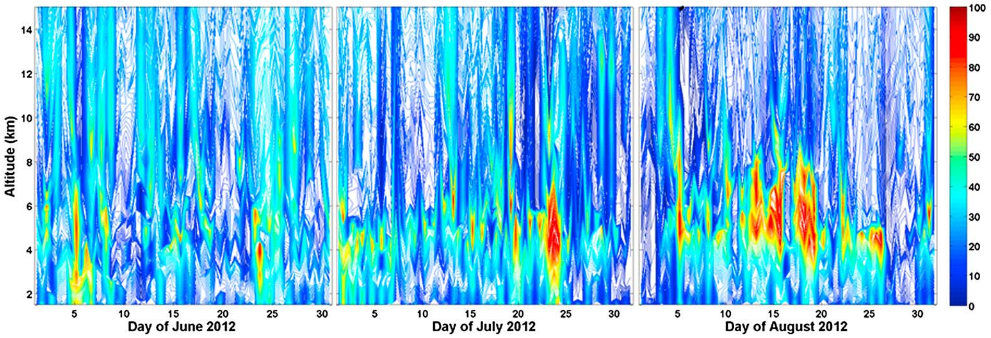

Figure 4. Vertical profile of relative humidity measured by balloon soundings of the Reno-National Weather Service at local times 5 A.M. and 5 P.M. The maximum altitude studied was 14 km. June and July experienced low relative humidity at ground and high levels. August presented less humidity at ground levels than at higher altitudes (around 6 km) on some days.

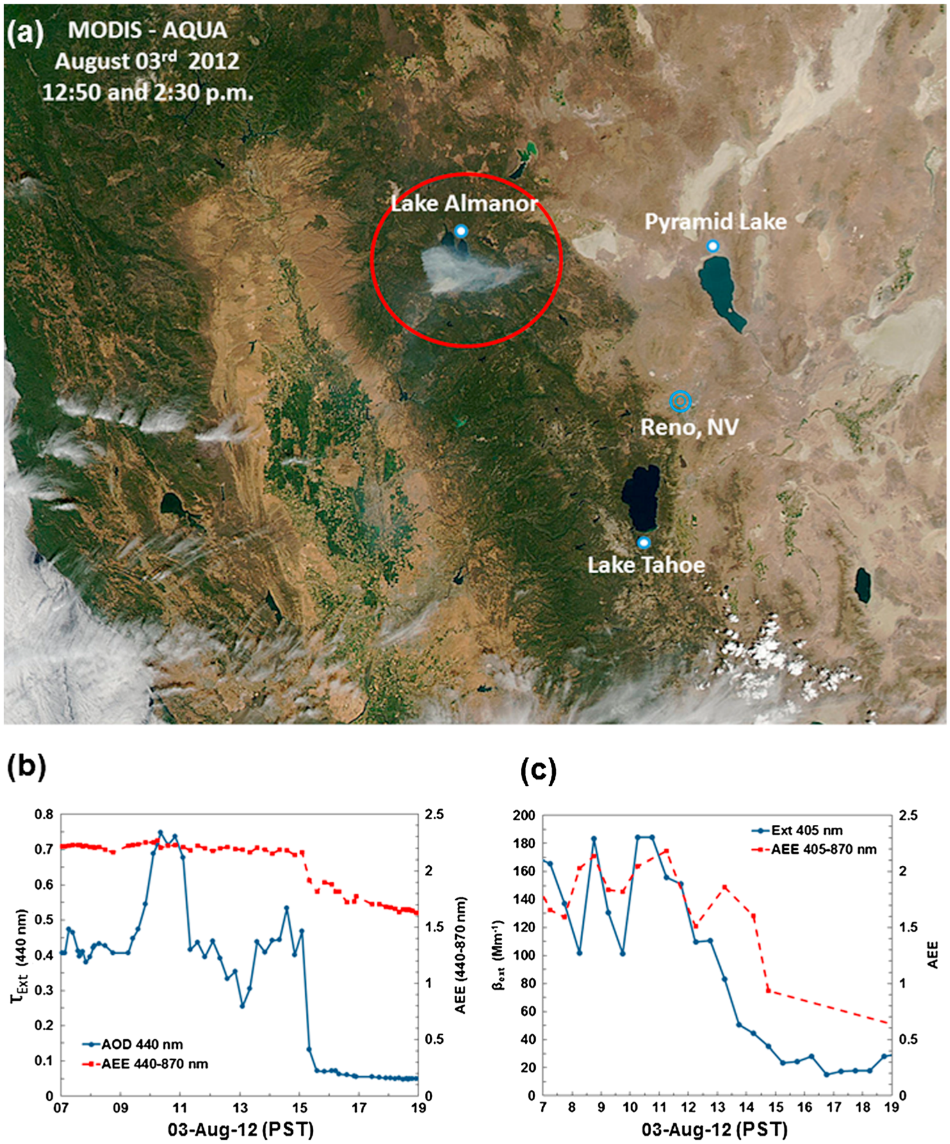

Figure 5. Chips fires near Lake Almanor, California. (a) MODIS image of smoke from the Chips fires near Lake Almanor, California, from Aqua satellite. The fire plume reached Reno, Nevada, on 3 August 2012. (b) AERONET (Level 1.0 data) τ_{ext} at 440 nm and AEE at 440–870 nm. (c) PIN (30 min averages) β_{ext} at 405 nm and AEE at 405–870 nm.

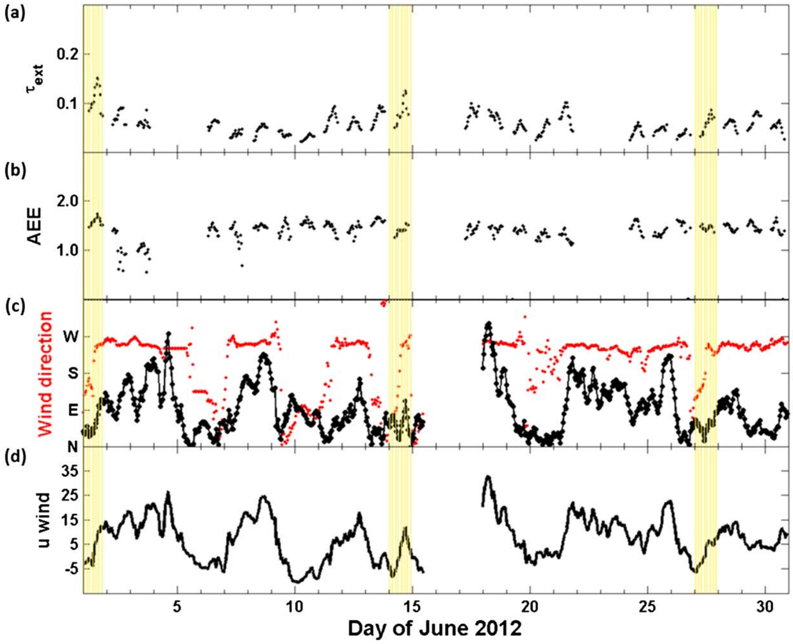

Figure 6. One hour averages for June 2012. Descending order: (a) AERONET τ_{ext} (500 nm), (b) AEE (440–870 nm Ångström extinction exponent), (c) wind direction (left axis red curve) and wind speed (right axis black curve, ms^{-1}), and (d) zonal wind speed (ms^{-1}). Yellow bars represent days with an increasing pattern of τ_{ext} in the afternoon.

mode aerosol is ventilated out, and coarse mode aerosol is present due to resuspension. If τ_{ext} increased with time, AEE decreased at the same time. June exposed lower values of AEE relative to the other 2 months. The lack of submicron aerosols was likely due to lower temperatures and higher winds at the very beginning of the month (Figures 1b and 1c). During the remainder of June, July, and August, AEE values varied,

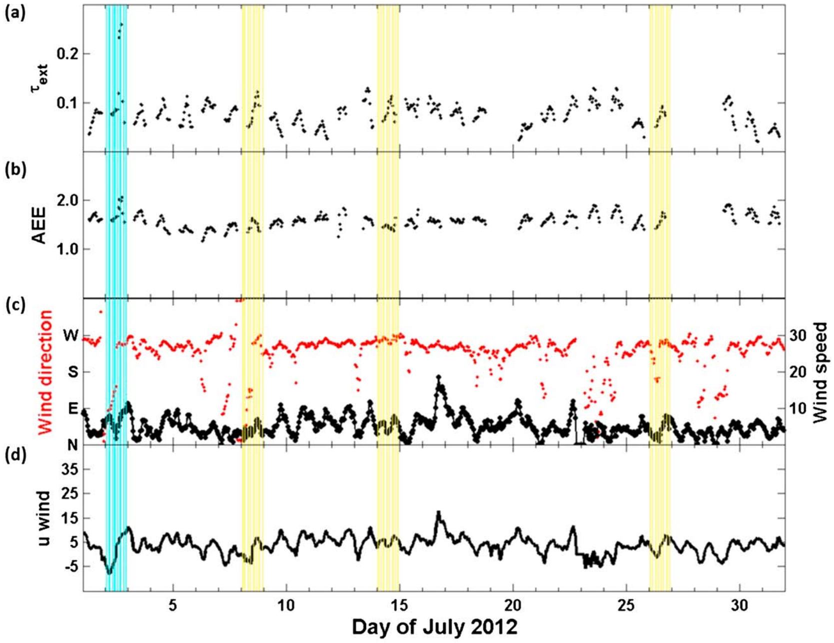

Figure 7. One hour averages for July 2012. Descending order: (a) AERONET τ_{ext} (500 nm), (b) AEE (440–870 nm Ångström extinction exponent), (c) wind direction (left axis red curve) and wind speed (right axis black curve, ms^{-1}), and (d) zonal wind speed (ms^{-1}). Yellow bars represent days during which a prolonged increase of τ_{ext} continued into the afternoon. Cyan bars represent the presence of wildfire smoke. Calm westerlies correlate to a prolonged increase in τ_{ext} into the afternoon.

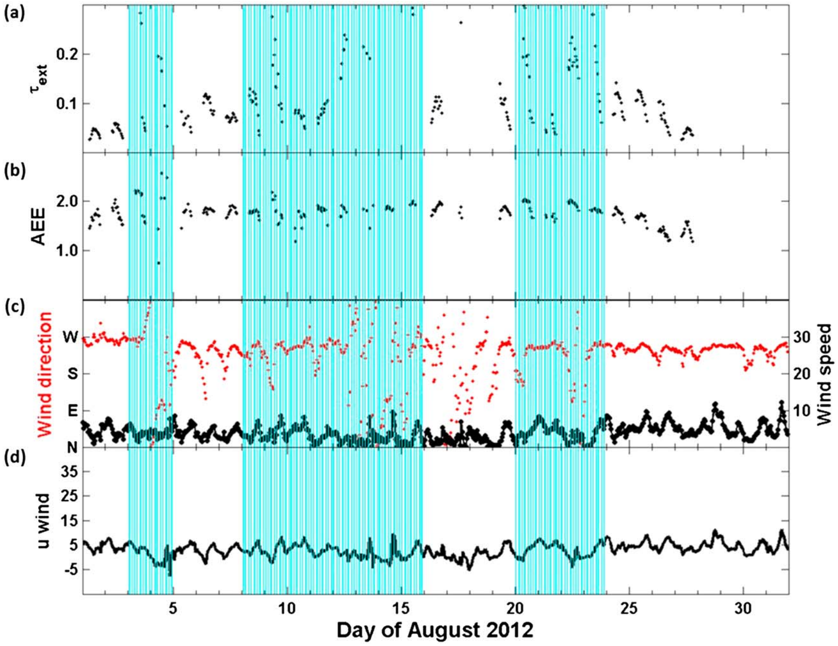

Figure 8. One hour averages for August 2012. Descending order: (a) τ_{ext} (500 nm), (b) AEE (440–870 nm Ångström extinction exponent), (c) wind direction (left axis red curve) and wind speed (right axis black curve, ms^{-1}), and (d) zonal wind speed (ms^{-1}). Cyan bars represent the impact of a wildfire. Absence of westerly flows contributed to cleaning the atmosphere in the afternoon when wildfires were present.

$1 < \text{AEE (440–870)} < 2$, indicating a mixture of coarse mode and fine mode contributions [*Schuster et al.*, 2006]. Additionally, regional forest fires contributed strongly to submicron aerosol levels during August as confirmed by back trajectory analysis and satellite imagery. AEEs in Figures 5b and 5c show that data from both instruments exhibited typical AEE values for biomass burning impacted (i.e., AEE ~ 2) [*Eck et al.*, 1999].

4.2. Zephyr Circulation and τ_{ext} Over Reno

Some days during June and July exhibited a prolonged increase of τ_{ext} with time during the day. August was primarily affected by fires, relegating this month to a special case distinct from the previous two. A relationship between wind speed and direction with τ_{ext} was found to be related to local circulation. The τ_{ext} peak in the afternoon, highlighted in yellow in Figures 6a and 7a, can be related to the Washoe Zephyr circulation. This section discusses a possible secondary aerosol transport and transformation mechanism that brings biogenically enhanced California Bay Area urban aerosol emissions over Reno.

The Washoe Zephyr circulation (WZC) is defined as a transition from easterly or weak wind speed to stronger westerly wind starting after noon [*Zhong et al.*, 2008]. Weak Pacific high pressure usually results in northerly flow in the morning hours during summer months. As the day warms, pressure changes between air masses in the elevated terrain of the Great Basin and those over Central California result in afternoon westerly winds in the lee of the Sierra Nevada Mountains [*Kingsmill*, 2000]. These pressure differences usually peak in the afternoon, forcing air from the west of the SNM crest down to the eastern slope. The Great Basin receives sunlight earlier in the morning than the SNM and is particularly dry in comparison to the SNM. More absorbed sunlight is partitioned to evapotranspiration (direct heating of the atmosphere) in the SNM (Great Basin); this also promotes the WZC.

Zhong et al. [2008] also hypothesized that the WZC would transport air pollution from the Central Valley to areas in the Great Basin; this was not tested at that time. According to Figures 6c, 7c, 6d, and 7d, the increasing τ_{ext} during afternoons, highlighted in yellow, during June and July occurred during a transition of negative (or low) to positive (or larger) *u* winds, consistent with the WZC. However, the WZC did not always explain τ_{ext} peaks in the afternoon, such as on the 14 July; τ_{ext} appears to be a much more complicated function of aerosol source strength and distribution, transformation during transport, and meteorology than is captured by the WZC alone.

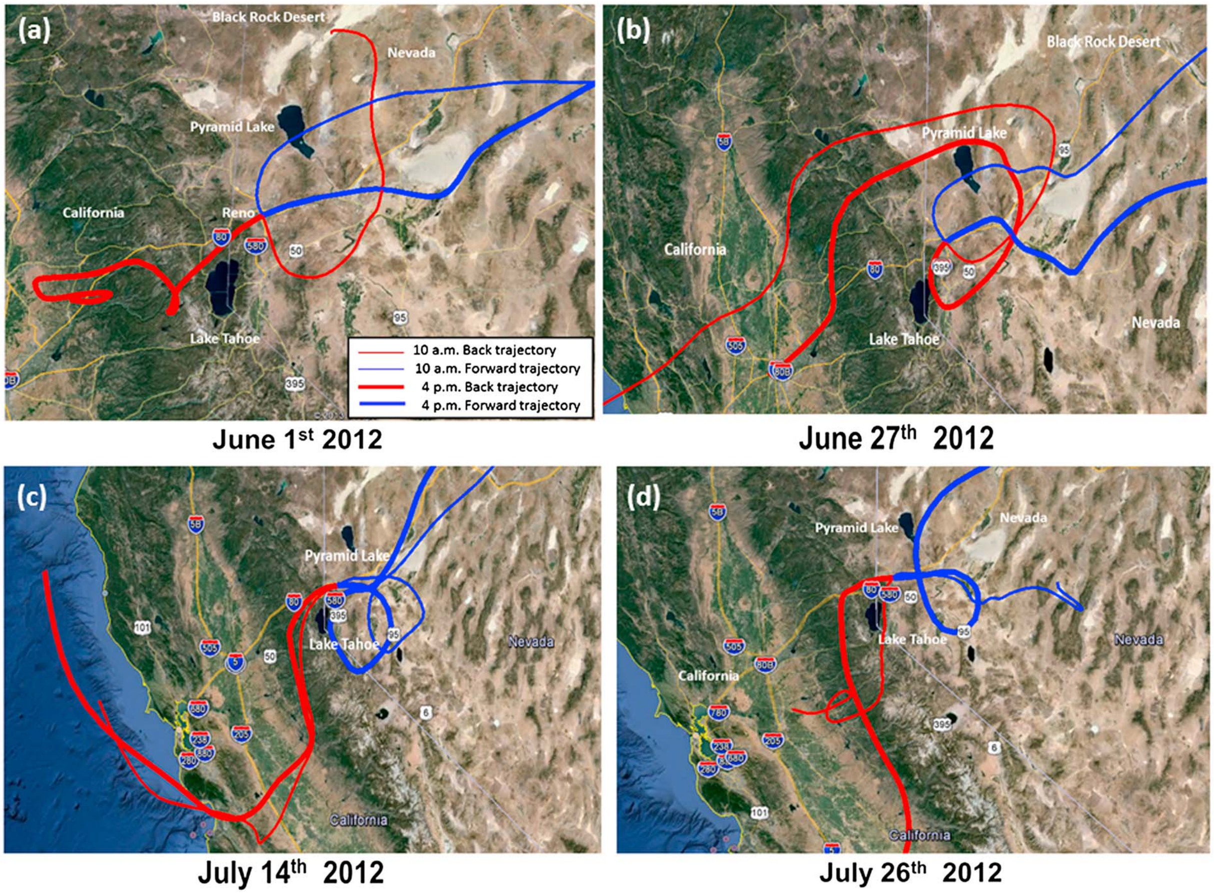

Figure 9. Hysplit model 500 m height back and forward trajectories at local times 10 A.M. and 4 P.M. over Reno. Thin red (blue) lines are back (forward) trajectories starting (finishing) at 10 A.M. local time. Thick red (blue) lines are back (forward) trajectories starting (finishing) at 4 P.M. local time. (a) 1 June 2012, (b) 27 June 2012, (c) 14 July 2012, and (d) 26 July 2012.

Light blue highlighting in Figures 7 and 8 represents the influence of known forest fires, with high levels of τ_{ext} and AEE in August. A common characteristic of those fires was that τ_{ext} in the morning was substantially higher than in the afternoon, likely due to plume direction changes rather than fire behavior.

Back and forward trajectory analysis using HySplit for the yellow highlighted days (1 and 27 June and 14 and 26 July 2012) are shown in Figure 9. Back (forward) trajectories start (end) 48 h before Reno. On 1 June (Figure 9a), the back trajectory shows that the air parcel that approached Reno at 10 A.M. (red thin line) came from the Black Rock Desert. The forward trajectory after 10 A.M., represented by the thin blue line, was blocked by the SMNs, and then it passed over Pyramid Lake and continued farther east. The thick red line shows that the back trajectory at 4 P.M. was drastically different from the 10 A.M. trajectory. During the afternoon, the air parcel which reached Reno came from the west (near Sacramento, California) and passed over I-80 and the SNMs, both important scenarios for traffic and biogenic emissions, respectively. The forward trajectory at 4 P.M. (thick blue line) shows a flow moving toward the east, consistent with the hypothesis that the WZC dominated the regional winds on this day.

Back trajectory analysis in the morning and afternoon for Reno on 27 June and 14 July (Figures 9b and 9c) showed trajectories from Central Valley, California, that passed over the SNMs and reached Reno. On 27 June, the afternoon back trajectory passed over both Pyramid Lake and Lake Tahoe before reaching Reno. The afternoon back trajectory on 26 July passed over the SNMs from Southern California before reaching Reno. All of the forward trajectories in Figures 9b, 9c, and 9d showed that the air parcels moved from Reno to the east. The spirit of the WZC is embodied in the flow pattern of Figure 9a but not in the others. In all these cases, the trajectories and aerosol sources intercepted are very complex and not easily generalized.

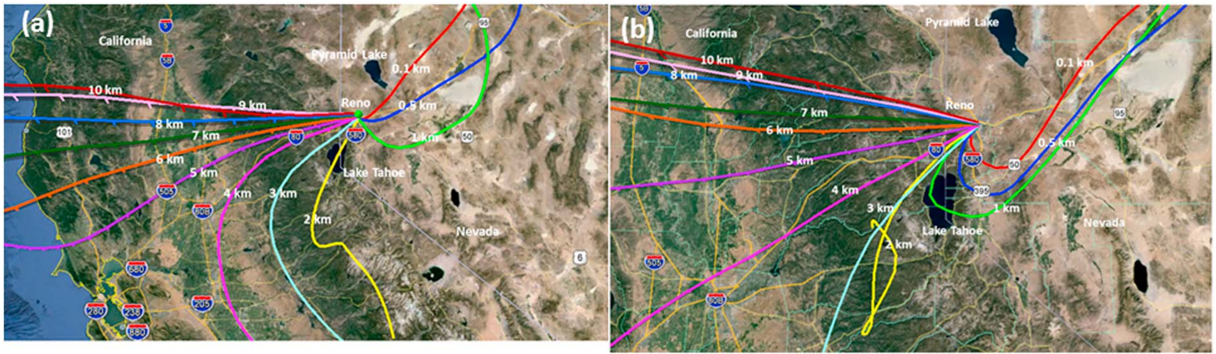

June 14th 2012
10:00 a.m. (PST)

June 14th 2012
4:00 p.m. (PST)

Figure 10. Hysplit model back trajectories to Reno on 14 June 2012 at 0.1 km, 0.5 km, 1 km, 2 km, 3 km, 4 km, 5 km, 6 km, 7 km, 8 km, 9 km, and 10 km. (a) Local time 10 A.M. The 2 km height trajectory passes over Lake Tahoe. (b) Local time 4 P.M. The 1 km height trajectory passes over Lake Tahoe.

Previous transport and chemical composition modeling coupled with observations during the CARES campaign in 2010 found that aerosols from the western side of the SNMs recirculated over Sacramento, generating layers of aged aerosol with feedback to the growth of the CBL the following day [*Fast et al.*, 2012]. Aerosol layers above the CBL were observed by the lidar on the B-200 aircraft over the west side of the SNMs as a result of recirculating patterns. The HySplit trajectory analysis made for representative days—1 June, 27 June, 14 July, and 26 July (Figure 9)—showed similar recirculation patterns as described in *Fast et al.* [2012], perhaps suggesting the possibility of aerosol above the CBL could be found at the eastern side of the SNMs.

Figure 10 presents the back trajectory analysis for 14 June at 10 A.M. and 4 P.M. from 200 m to 10 km above ground level (agl) to explore the vertical structure of the WZC. Figure 10a presents the morning near-ground (0.1, 0.5, and 1 km agl) back trajectories at 10 A.M. with easterly flows consistent with weak or nonexistent WZC. Comparison of the near-ground trajectories at 4 P.M. shows that the wind flow at these levels becomes more westerly in the afternoon, consistent with the WZC. High levels (above 1 km) display the westerly flow characteristic of the synoptic scale where the WZC influence is less apparent.

4.3. Diel Averages and Aerosol Optical Properties

The apparent optical height (AOH) is defined as the ratio between the τ_{ext} (Cimel CE-318 at 440 and 870 nm) and the near-surface aerosol extinction coefficient (PIN at 405 and 870 nm) as

$$\mathrm{AOH}(\lambda) = \tau_{\mathrm{ext}}(\lambda)/\beta_{\mathrm{ext}}(\lambda) \tag{1}$$

AOH is a length scale to represent the height below which aerosols are distributed within the atmosphere. Under the circumstance of height-independent extinction within the boundary layer and no aerosol extinction in the free atmosphere above, AOH is equal to the CBL layer height.

The basic idea is that the AOH and height of the CBL should be similar as a necessary condition for direct, quantitative use of remote sensing measurements to determine near-surface aerosol pollution levels. In this case, aerosols in the CBL represent surface conditions, and negligible aerosols are located in the free atmosphere above the CBL.

Further, measurements (from June 2006 to September 2009) in Illinois (by using in situ vertical profile data from meteorological aircraft) demonstrated that aerosol light extinction was mostly confined to the CBL and that aerosol intrinsic parameters such as AEE and SSA did not substantially vary through the vertical [*Sheridan et al.*, 2012]. Results from that campaign, including that aerosol at higher altitudes is less hydroscopic and more strongly absorbing at shorter wavelengths, suggest dust as the dominant aerosol. In addition, aerosols in the mixed layer were darkest (low single scattering albedo). A March aircraft campaign from Sacramento, California, NE over the Sierra Nevada mountains north of SMN showed that cloud condensation nuclei concentrations (here a proxy for light scattering aerosol concentration) were mostly found in the CBL as it developed from morning to afternoon [*Rosenfeld et al.*, 2008].

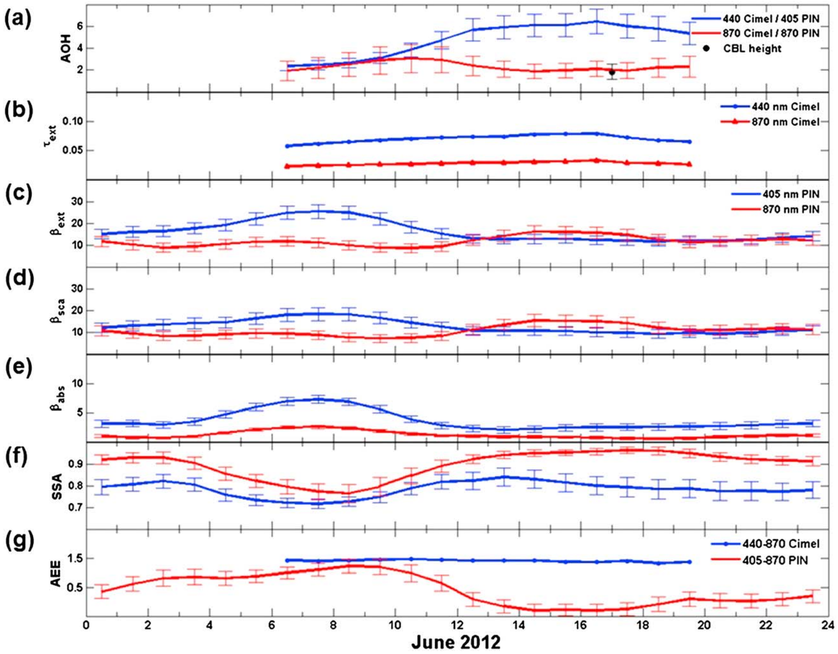

Figure 11. Diel averages of in situ and remotely sensed aerosol optical properties for June 2012 in Reno measured by PIN and Cimel CE-318. Descending order: (a) Apparent optical height (km) at 440–405 nm and 870–870 nm. Convective boundary layer height at 5 P.M. retrieved from the Reno-National Weather Service balloon soundings. (b) Entire column aerosol optical extinction at 405 and 870 nm, (c) ground-level aerosol light extinction coefficient (Mm^{-1}) at 405 and 870 nm, (d) ground-level aerosol light scattering coefficient (Mm^{-1}) at 405 and 870 nm, (e) ground-level aerosol light absorption coefficient (Mm^{-1}), (f) ground-level SSA at 405 and 870 nm, and (g) AEE at 440–870 nm (entire column) and at 405–870 nm (ground level). Uncertainty on each plot was determined by assuming 5% and 15% of relative uncertainty in photoacoustic and nephelometer measurements, respectively, and 1% of relative uncertainty in the AERONET algorithm, and propagation error equations were associated with each parameter.

The wavelength dependence of AOH is useful to infer the scale height of submicron and supermicron aerosol. The volumetric extinction efficiency for 405 nm peaks in the fine mode size range while 870 nm efficiency extends into the coarse mode, as discussed further in Appendix B. Figures 11a, 12a, and 13a show the diel average of AOH for predominantly submicron aerosols (440 nm Cimel – 405 nm PIN) and predominantly supermicron particles (870 nm Cimel – 870 nm PIN) for June, July, and August.

Referring to Figure 11a, AOH for fine particles (440 nm curve) in June exhibited a maximum of 6.4 km at 4 P.M. Meanwhile, coarse aerosol AOH associated with 870 nm peaked at 3 km at 10 A.M. According to the balloon soundings, the diel average of CBL height was 1.8 ± 0.7 km at 5 P.M. in June 2012. It is likely that June was characterized by fine mode secondary aerosol formation well above the surface as the day progressed, in reference to the 440 nm curve. AOH from coarse particles agreed with the height of the CBL while AOH from fine particles was higher than the CBL height.

AOH in July for small particles peaked at 4.8 km at 3 P.M.; in contrast, large particle AOH peaked at 3.8 km at noon. The diel average of CBL height according to balloon soundings was ~2.5 ± 0.7 km at 5 P.M. in July. AOH at 5 P.M. was higher for the 440–405 nm relationship and agreed for the 870 nm calculation, implying that at 5 P.M. the coarse mode could be confined in the CBL height but that part of the fine mode was found above it. We infer that coarse particles were largely confined to the CBL. By contrast, fine particles were found in concentrations not explainable by surface conditions alone, either due to formation or transport of submicron aerosol into the upper CBL or above it. Aerosol transport is likely related to afternoon westerly winds perhaps due to episodes of the WZC.

August AOH is dominated by fire conditions. Small particle AOH peaked at 4.95 km at 2 P.M., whereas large aerosol AOH did so at 2.94 km at 1 P.M. In situ PIN and entire column Cimel instruments perceived the fire signal especially strongly in the morning hours. The diel average of the CBL height retrieved from the balloon soundings was 2.6 ± 0.8 km at 5 P.M. in August. This result shows that the coarse particles were confined within

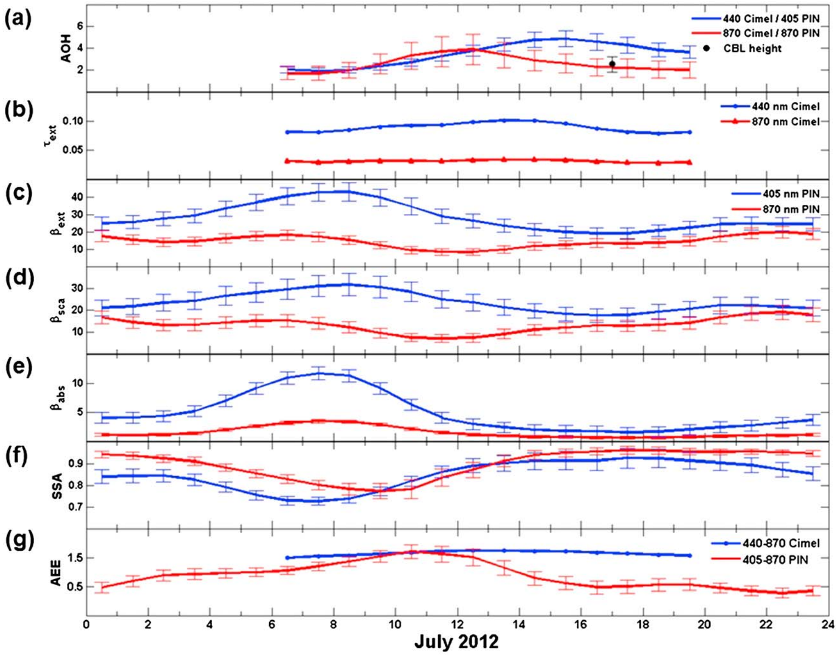

Figure 12. Same as Figure 11 but for July 2012.

the CBL at 5 P.M. but some portion of the fine mode was found above the CBL. Wind direction change and speed increase acted as a local cleansing mechanism. Most of the fire episodes were related to the absence of westerly flow (WZC) in the afternoons. The afternoon fine mode aerosols aloft give rise to larger than expected AOH, even for the fire-affected month of August.

By comparison, in relatively flat, midcontinental terrain, the Illinois results [*Sheridan et al.*, 2012] showed that most fine particles were generally confined to the CBL. AOH results in Reno were much more complicated because of the differences in geography with the presence of the SNMs that allows air pollution to enter the

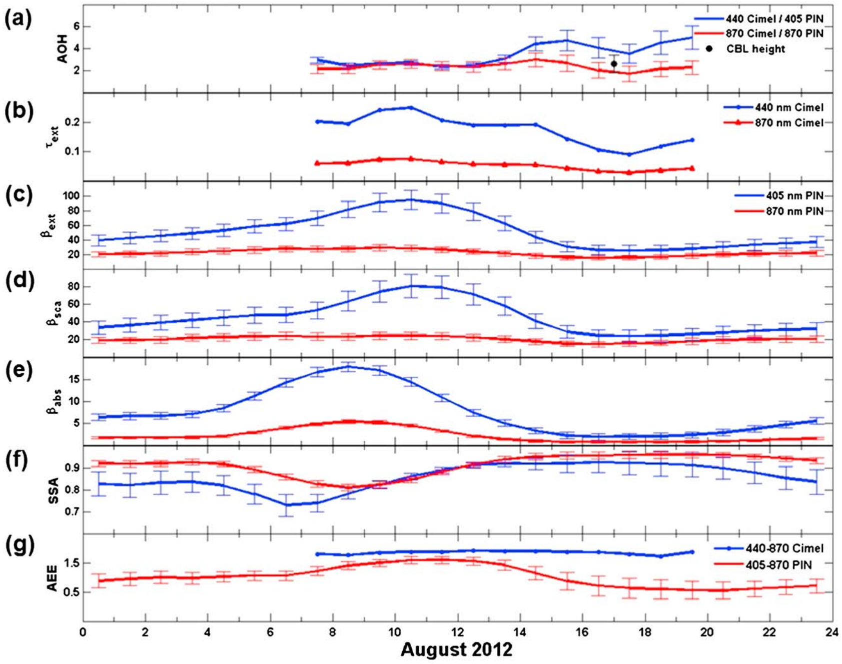

Figure 13. Same as Figures 11 and 12 but for August 2012.

free atmosphere near the mountain crest. Reno presents desert weather conditions that have low evapotranspiration and hygroscopic growth aloft. Finally, high temperatures along with biogenic emissions from forests promote secondary aerosol formation and transport over Reno.

A 2 year campaign using a Cessna 172XP aircraft from March 2000 was performed to study the seasonal aerosol vertical profile over Department of Energy's (DOE) Southern Great Plains, Oklahoma [*Andrews et al.*, 2011]. During this campaign, they found that aerosol extinction coefficients decreased sharply with increasing altitude below 1.5 km and thereafter less sharply until the aircraft maximum altitude of 5 km. A coastal study in Singapore using Micro Pulse Lidar showed that smoke plumes were generally confined within 2−3 km of the surface [*Chew et al.*, 2013]. In addition, they found that the sources of aerosol above (~4 to ~6 km) are highly variable compared with those near the surface. The aerosol in elevated layers over Singapore was transported there by substantial vertical wind shear. Results over Reno during fire conditions (August 2012) were qualitatively similar to the fire cases in Singapore where the fire plumes were confined within the first 3 km above ground level. Substantial aerosol optical depth above the CBL was found as well in Singapore as was observed over Reno, although likely due to different mechanisms.

Diel average for τ_{ext} and aerosol light extinction coefficient (β_{ext}) in Figures 11b, 12c, 13b, 11c, 12b, and 13c were calculated in order to compare aerosol column with aerosol ground measurements. June τ_{ext} and β_{ext} (Figures 11b and 11c, respectively) measurements agreed when both instruments exhibited low aerosol pollution conditions. However, aerosol column and ground observations differed during the day. June τ_{ext} had maxima (0.08 at 440 nm and 0.03 at 870 nm) at 4 P.M. when secondary organic aerosol dominated the air pollution. β_{ext} coefficient peaked (25.4 Mm^{-1} at 405 nm and 16.1 Mm^{-1} at 870 nm) at 8 A.M. when primary local vehicular emissions influenced the concentration of aerosols. In situ β_{ext} observations at 870 nm were higher than those at 405 nm for the afternoon in June, likely due to the higher wind speed in this month. Further discussion of the June β_{ext} comparison at 870 nm and at 405 nm is presented in Appendix B.

July results (Figure 12) are somewhat similar to those of June. τ_{ext} peaked (0.10 at 440 nm and 0.03 at 870 nm) at 2 P.M., whereas β_{ext} (42.9 Mm^{-1} at 405 nm and 19.9 Mm^{-1} at 870 nm) was influenced, as in June, by the local rush hour and peaked at 8 A.M. July τ_{ext} at 440 nm peaked somewhat more dramatically and earlier by a few hours than June, perhaps due to the more dominant influence of secondary aerosol in July. Additionally, β_{ext} PIN measurements for July agreed with previous results in nonsmoky conditions of August 2008 [*Gyawali et al.*, 2009].

August AOH shown in Figure 13a is closer in value to the height of the CBL (≈3 km) until noon. Comparing with Figures 11a and 12a, it can be seen that the 405/440 nm AOH diverges less from the expected height of the CBL in the afternoon in comparison with June and July AOH. The τ_{ext} shown in Figure 13b is higher in August than the other months due to smoke in Reno from California fires. Apparently, the smoke was confined mostly to the CBL. Both τ_{ext} (0.25 at 440 nm and 0.07 at 870 nm) and β_{ext} (94.5 Mm^{-1} at 405 nm and 29.1 Mm^{-1} at 870 nm) peaked at 10 A.M.

Near-surface aerosol light scattering (β_{sca}) and aerosol light absorption (β_{abs}) coefficients are shown in Figures 11d, 11e, 12d, 12e, 13d, and 13e. The predominance of scattering in the total extinction is shown in June and July measurements (Figures 11d and 12d); β_{sca} and β_{abs} peaked around the same time, and they were affected by local primary motor vehicle emissions during the rush hour (6–9 A.M.). The scattering signal at 870 nm is higher than those at 405 nm during June as discussed in Appendix B. Higher levels of urban aerosol pollution during July (with respect to June) exhibited a larger contribution of fine particles to the optics. Scattering and absorption in August (Figures 13d and 13e) showed similarities with the Mexico City MILAGRO campaign of 2006 [*Paredes-Miranda et al.*, 2009]. During August, absorption peaked during the rush hour due to primary sources and though scattering peaked later in the morning (10 A.M.) likely as a result of photochemical interactions producing secondary aerosol.

Single scattering albedo (SSA) is the ratio between aerosol light scattering and aerosol light extinction and is measured by the PIN. AERONET retrieval for SSA was not used because of the high uncertainty associated with low τ_{ext} ($\tau_{\mathrm{ext}} = 0.4$ at 440 nm is the threshold below which SSA determination is taken to be invalid). Figures 11f, 12f, and 13f depict the contrasts between SSA for the months of June, July, and August, during which aerosol absorption was dominated by vehicular emissions and wildfire aerosols. The figures

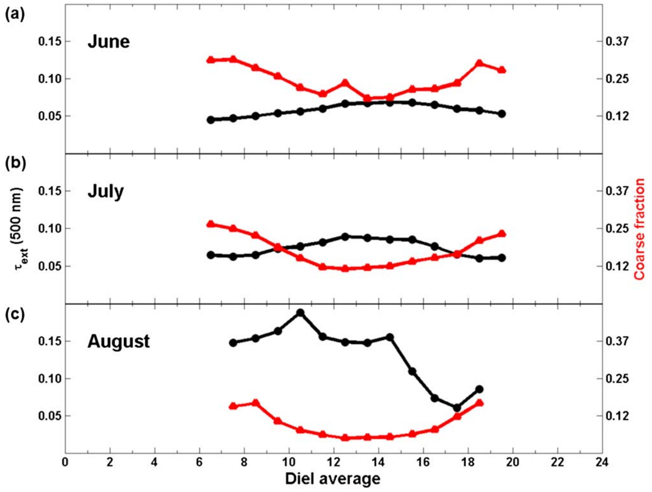

Figure 14. Diel averages of τ_{ext} were measured at 500 nm (left axis). Diel averages of the coarse fraction (right axis). (a) June 2012, (b) July 2012, and (c) August 2012. The averages in July and August take into account fire and nonfire days.

also expose differences and similarities with the work of *Gyawali et al.* [2009]. In general, SSA was greater at 870 nm than at 405 nm, perhaps due to the contribution of nonfine mode dust that absorbs more strongly at shorter wavelengths. July 2008 [*Gyawali et al.*, 2009] was a much smokier month than August 2012.

SSA at 405 nm ranged from 0.72 to 0.84 during June, from 0.73 to 0.92 during July, and from 0.76 to 0.93 during August. SSA at 870 nm was substantially higher than SSA at 405 nm. SSA at 870 nm varied from 0.76 to 0.96 during June, from 0.77 to 0.96 during July, and from 0.81 to 0.96 during August. Strong diurnal variation of SSA was observed with minima during the morning rush hour (6–9 A.M.) and maxima on either side. Photochemical reactions during daytime might have increased scattering coefficients of the aerosol, causing the higher SSA values at both wavelengths for the latter part of the day.

Figures 11g, 12g, and 13g depict AEE diel averages calculated at 405–870 nm for PIN and 440–870 nm for AERONET retrievals. Ground-based measurements (PIN) exhibited a maximum of AEE in the morning, followed by a decrease during the remainder of the day; this pattern was found in all 3 months of the study. In contrast, column measurements (Cimel CE-318) remained flat over the same time period. Readings from both instruments matched in the morning when primary emission dominated aerosol optical properties. However, secondary aerosol was likely perceived by Cimel CE-318, while PIN observed the contribution of supermicron (AEE ~ 1). June (Figure 11g) presented lower and sometimes negatives AEE values than the later months due to high wind speed, lower temperatures, and contribution of dust in the optics. In contrast, AEE observed in July (Figure 12g) increased due to calm winds and higher temperatures. August (Figure 13g) showed the highest AEE (AEE > 2) due to the impact of wildfires in California. Cimel CE-318 detected the typical values for atmospheric aerosols (1 < AEE < 2).

4.4. Coarse Fraction

The coarse fraction (CF) is the ratio between coarse mode particle optical depth and total optical depth in the atmosphere column viewed by the Sun photometer at a particular time. It quantifies a fraction of τ_{ext} associated with supermicron particles in the air. This factor is retrieved throughout the day by Cimel/AERONET from direct Sun scans, and it is a quantitative alternative of AEE for inferring particle size [*Eck et al.*, 2003].

Figure 14 illustrates the diel average of τ_{ext} at 500 nm (left axis) and coarse fraction (right axis) for local summer months. In general, τ_{ext} and CF are inversely related; as τ_{ext} increased, CF decreased and vice versa (Figures 14a and 14b). The reason for this inverse relationship is likely that in the middle of the day, secondary aerosol formation increased production of fine particles, decreasing CF. Overall, June was more influenced by coarse particles than the latter 2 months, likely due to windier and cooler conditions. Appendix B further discusses retrieved aerosol size distributions. Previous studies during the CARES campaign in 2010 reported significant coarse fraction (especially from sea salt) transported from the Pacific Ocean to the Central Valley California [*Zaveri et al.*, 2012; *Kassianov et al.*, 2012]. In relation to June 2012, part of the coarse mode found in Reno, Nevada, may have been from local production and some part could have been transported over the SNMs. However, chemical composition and transport modeling studies must be conducted in order to clarify these hypotheses. Finally, fire smoke transported from California to Reno dominated the fine mode in August (Figure 14c).

5. Conclusions

Averaged ground-based and columnar measurements of light extinction and τ_{ext}, respectively, showed June as the cleanest month due to higher wind speed and lower temperatures that acted as local cleaning mechanisms with respect to the two latter months. The influence of forest fires in California, high temperatures, and calm winds increased aerosol concentrations in August beyond those in June and July. Also, in August, AEE revealed submicron particles when wildfire smoke was transported into the Reno area.

Low wind speed and westerly flow episodes of Zephyr circulation enhanced aerosol concentrations during some June and July afternoons. Air pollution from wildfires did not persist during the afternoon when nonwesterly flow periods of Zephyr circulation were present.

Extinction coefficients measured by the PIN instrument showed that the maximum air pollution contribution was due to local vehicular emissions during morning rush hour. However, Cimel CE-318 observations pointed out that secondary aerosols dominated aerosol optics during June and July afternoons. Data from both instruments suggested that fire conditions during August mornings strongly influenced aerosol properties in the atmosphere. SSA measurements suggested that aerosol light absorption was largest during the morning rush hour and aerosol light scattering during the remainder of the day.

The coarse mode fraction obtained from direct Sun photometer measurements diminished during June and July afternoons due to secondary aerosol formation and in August due to the presence of fire smoke.

AOH retrieved for 440–405 nm was unrealistically very large compared to typical expected values of the CBL height. However, AOH retrieved for 870–870 nm showed some correspondence with observed CBL height due to the enhanced coarse particles contribution that is more likely confined to the boundary layer.

Particle extinction coefficients were commensurate with aerosol being primarily emitted into the boundary layer during morning hours. However, during the afternoon, higher levels of the atmosphere may have enhanced extinction and/or the boundary layer is not uniformly filled with aerosol (secondary submicron aerosol is not as prevalent at the surface). Therefore, the ability of column-integrated remote sensing to measure near-surface local aerosol pollution in Reno (and Reno-like cities) is best during morning hours and is complicated during afternoons.

A recent paper hypothesizes that a cooling haze of secondary organic aerosol develops over the southeastern U.S. in summer months from the photochemical interaction of anthropogenic air pollution with biogenic volatile organic compounds emitted by forests [*Goldstein et al.*, 2009]. It is very likely that such a mechanism produces the fine mode aerosol reported here that appears to be concentrated above surface extinction instruments. The Sacramento and San Francisco Bay areas are sources of anthropogenic air pollution that has been observed to produce enhanced secondary aerosol formation aloft in the foothills of the Sierra Nevada mountains downwind of Sacramento [*Shilling et al.*, 2013]. A systematic increase in fine mode scattering coefficient at 355 nm and 405 nm during the progressively warmer months was observed at the ground during this campaign as well [*Gyawali et al.*, 2013]. This aerosol plume is often brought over the Sierra Nevada mountains to Reno by the WZC in the afternoon hours and is likely the source of the enhanced column aerosol optical depth we observed in this study. Thus, it appears that the cooling haze discussed by *Goldstein et al.* [2009] is important in the western U.S. as well, as an aerosol formation mechanism with an important climate impact. The mechanism of fine mode AOD enhancement may be secondary aerosol formation above the surface and/or CBL as well as depletion of the fine mode by the coarse mode through coagulation and condensation of precursor gases near the surface. Further work is needed to identify the vertical distribution of fine and coarse mode AOD and its chemistry.

Appendix A: Data Smoothing and Measurement Uncertainty

A Savitzky-Golay smoothing algorithm was applied to the PIN diel averages. The equation employed the following:

$$Y_i = \frac{1}{231}\left[-21\,y_{i-4} + 14\,y_{i-3} + 39\,y_{i-2} + 54\,y_{i-1} + 59\,y_i + 54\,y_{i+1} + 39\,y_{i+2} + 14\,y_{i+3} - 21\,y_{i+4}\right], \qquad \text{(A1)}$$

where Y_i is the quadratic/cubic polynomial smoothing with nine coefficients for smoothing [*Savitzky and Golay*, 1964]. Periodic boundary conditions were assumed for the transition around midnight.

Diel averages should be formed from a diurnal pattern that has been repeated multiple times under the same circumstances throughout a period of time. During the experiment, the daily variability of aerosol concentration and measurement imprecision (noise) both contributed to variation. The detrended Standard Deviation (ΔS), aimed at quantifying measurement imprecision, was calculated by the following:

$$\Delta S(y) = \pm\sqrt{\frac{\left(\sum_{i=1}^{N}\left(y^i - y^i_{\text{smooth}}\right)\right)^2}{N}} \tag{A2}$$

where y^i is the result of diel averaging, y^i_{smooth} is the data after being smoothed using equation (A1), and N is the total number of entries in the data set.

The uncertainty associated with measurements of the absorption coefficient is obtained from the following:

$$\Delta\beta_{\text{abs}} = \pm\sqrt{\left(\Delta S(\beta_{\text{abs}})\right)^2 + \left(\Delta a\,\beta^{\text{smooth}}_{\text{abs}}\right)^2} \tag{A3}$$

where $\Delta S(\beta_{\text{abs}})$ is the uncertainty related to the absorption measurement and Δa is the photoacoustic relative uncertainty due to calibration inaccuracy. At 405 nm, the magnitude of the error bars was from 0.57 to 0.67 Mm^{-1} (June), from 0.9 to 1.07 Mm^{-1} (July), and from 0.71 to 1.13 Mm^{-1} (August). For 870 nm, the uncertainty was lower due to use of a higher-power laser at this wavelength compared with 405 nm (factor of 4 higher laser power). The magnitude of the error bars varied from 0.23 to 0.26 Mm^{-1} (June), from 0.23 to 0.29 Mm^{-1} (July), and from 0.25 to 0.37 Mm^{-1} (August). June exhibited lower uncertainty at both wavelengths due to low levels of aerosol. In contrast, wildfires in August increased the aerosol concentration, and therefore, the absolute error increased.

A similar relationship as equation (A3) was used for the scattering coefficient uncertainty as follows:

$$\Delta\beta_{\text{sca}} = \pm\sqrt{\left(\Delta S(\beta_{\text{sca}})\right)^2 + \left(\Delta s\,\beta^{\text{smooth}}_{\text{sca}}\right)^2} \tag{A4}$$

where ΔS(sca) is the uncertainty related to the scattering measurement and Δs is the nephelometer relative uncertainty. The uncertainty ranges calculated at 405 nm were from 1.9 to 3.0 Mm^{-1} (June), from 3.1 to 5.0 Mm^{-1} (July), and from 6.6 to 13.3 Mm^{-1} (August). Light scattering coefficient measurements had an uncertainty from 1.9 to 2.8 Mm^{-1} (June), from 2.0 to 3.3 Mm^{-1} (July), and from 3.0 to 4.2 Mm^{-1} (August). This increasing trend observed for each is due to the higher aerosol concentration during morning rush hour and because of the aerosol increase likely that is due to secondary aerosol formation associated with higher temperatures and lower wind speeds in July and August.

The equation for the error in the extinction coefficient is as follows:

$$\Delta\beta_{\text{ext}} = \pm\sqrt{\left(\Delta S(\beta_{\text{sca}})\right)^2 + \left(\Delta S(\beta_{\text{abs}})\right)^2 + \left(\Delta s\,\beta^{\text{smooth}}_{\text{sca}}\right)^2 + \left(\Delta a\,\beta^{\text{smooth}}_{\text{abs}}\right)^2} \tag{A5}$$

where scattering and absorption uncertainty contribute to the calculation of β_{ext} uncertainty. $\Delta\beta_{\text{sca}}$ generally dominates the β_{ext} propagated error. The ranges for 405 nm were from 2.0 to 3.1 Mm^{-1} (June), from 3.2 to 5.1 Mm^{-1} (July), and from 6.7 to 13.3 Mm^{-1} (August). At 870 nm, uncertainty varied from 1.9 to 2.8 Mm^{-1} (June), from 2.0 to 3.3 Mm^{-1} (July), and from 3.0 to 4.2 Mm^{-1} (August).

The uncertainty equation for AOH is as follows:

$$\Delta\text{AOH} = \pm\text{AOH}\sqrt{\left(\frac{\Delta\beta_{\text{ext}}}{\beta_{\text{ext}}}\right)^2 + \left(\frac{\Delta\tau_{\text{ext}}}{\tau_{\text{ext}}}\right)^2}. \tag{A6}$$

The uncertainty associated with AOH relates β_{ext} and τ_{ext} relative uncertainties for PIN and Cimel CE-318, respectively. For the submicron relationship, the uncertainty in AOH varied from 0.4 to 1.1 km (June), from 0.3 to 0.8 km (July), and from 0.2 to 1.1 km (August). The uncertainty for the 870 nm coarse particle AOH varied from 0.7 to 1.3 km (June), from 0.6 to 1.4 km (July), and from 0.4 to 0.7 km (August). These values are 23 to 43% of the measured values.

Single scattering albedo, SSA, (represented here by ω_0) has an uncertainty equation as follows:

$$\Delta\omega_0 = \pm\,\omega_0(1-\omega_0)\sqrt{\left(\frac{\Delta\beta_{\text{abs}}}{\beta_{\text{abs}}}\right)^2 + \left(\frac{\Delta\beta_{\text{sca}}}{\beta_{\text{sca}}}\right)^2} \tag{A7}$$

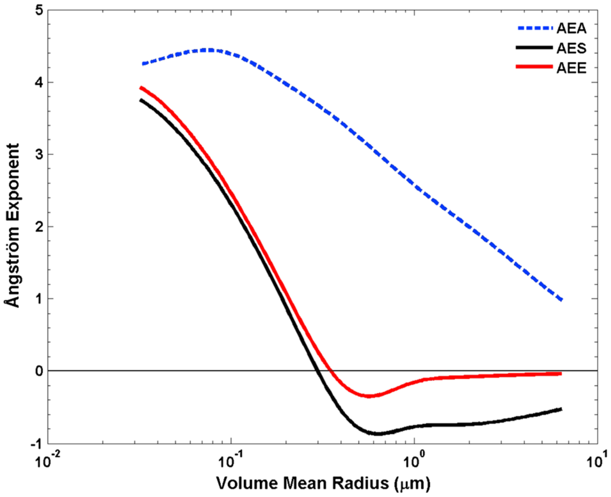

Figure B1. Ångström exponents for the dust model.

that relates $\Delta\beta_{sca}$, $\Delta\beta_{abs}$, β_{sca}, and β_{abs} relative uncertainties and observations, respectively. At 405 nm, the uncertainty in SSA measurements varied from 0.02 to 0.05 (June), from 0.02 to 0.04 (July), and from 0.01 to 0.03 (August), which is from 1 to 6% of the measured values. At 870 nm, the uncertainty ranges were from 0.01 to 0.04 (June), from 0.02 to 0.04 (July), and from 0.01 to 0.02 (August). This data uncertainty is from 1 to 5% of the measured values.

The AEE uncertainty equation relates extinction coefficient measurements and extinction coefficient uncertainties at 405 and 870 nm by the following equation:

$$\Delta\mathrm{AEE} = \pm\frac{\sqrt{\left(\frac{\Delta\beta(\lambda_1)_{\mathrm{ext}}}{\beta(\lambda_1)_{\mathrm{ext}}}\right)^2 + \left(\frac{\Delta\beta(\lambda_2)_{\mathrm{ext}}}{\beta(\lambda_2)_{\mathrm{ext}}}\right)^2}}{\ln(870/405)}. \tag{A8}$$

The ranges for AEE uncertainties were from 0.2 to 0.3 (June), from 0.1 to 0.3 (July), and from 0.1 to 0.3 (August). These represent from 20 to 66% of data variability.

Appendix B: Clarification of June Aerosol Optical Properties

B1. Dust Ångström Exponent's Model

Figure B1 shows a dust-aerosol model of the Ångström Exponent of Absorption (AEA), Ångström Exponent of Scattering (AES), and Ångström Exponent of Extinction (AEE). The refractive index for 405 nm was taken to be $n_r = 1.53$ and $n_i = 0.03$, while the refractive index for 870 nm was $n_r = 1.53$ and $n_i = 0.003$. The AEA peaks at 0.1 μm due to enhanced size-dependent absorption at 405 nm. AES (AEE) becomes negative when the volume mean radius is approximately 0.3 (0.35) μm. The minimum value for AEE approaches -1 and negative thereafter, as particle size increases as a consequence of stronger absorption at 405 nm. Thus, Figure B1 displays the feasibility of having negative AEE for a commonly used choice of dust refractive indices and is likely the explanation for the small AEE values observed in June 2012 (Figure 11g). A study made over North Africa and the Arabian Peninsula similarly revealed that the columnar AEE retrieved by AERONET reached values very close to zero [*Kim et al.*, 2011].

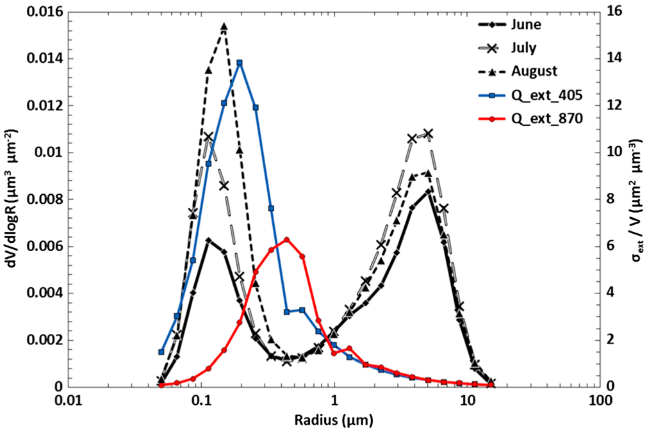

Figure B2. Left *y* axis: AERONET columnar volume size distribution average versus radius for June, July, and August 2012. Right *y* axis: extinction cross section per unit volume for the dust model.

Monthly averages of size distributions retrieved from AERONET (Level 2 data) for June, July, and August are shown in Figure B2 (left axis). June displayed a significant dominance of the coarse mode due to dusty and windy conditions present during the seasonal transition. July was equally dominated by fine and coarse particles. Because of the fire plumes and calmer wind speed, August was substantially dominated by the fine mode.

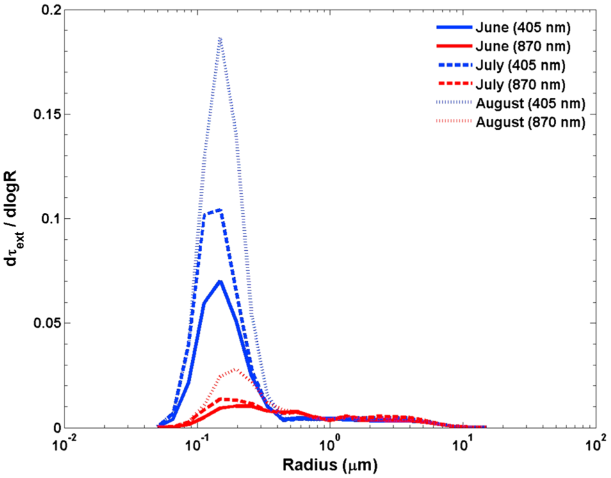

Figure B3. Distribution of extinction optical depth.

The particle volumetric extinction efficiency (extinction cross section divided by particle volume) at 405 and 870 nm from the dust model is shown in Figure B2 (right axis). The volumetric extinction efficiency at 405 nm is almost dominated by the fine mode peaking at 0.2 μm. Meanwhile, the volumetric extinction efficiency at 870 reveals contribution from both fine and coarse modes peaking at 0.5 μm.

Figure B3 shows the distribution of extinction optical depth, $d\tau_{ext}$/dlogR, that is the product of the columnar volume size distribution (retrieved from AERONET) and the volumetric extinction efficiency at 405 and 870 nm from the dust model. The area under these curves is τ_{ext} at 405 and 870 nm during June, July, and August 2012. June presented the cleanest conditions, and August was the most polluted. June also had the largest coarse mode fraction (Figure 14), a quantity determined from the spectral AOD measurements. The 405 nm contributions are mostly from the fine mode and the 870 from both fine and coarse modes, especially for June. Figure B3 makes use of the retrieved size distribution for the entire column. The near-surface size distribution may differ from the column averaged value.

B2. AEA

AEA represents the wavelength dependence of absorption; the equation for the AEA at 405 and 870 nm can be written as follows:

$$\mathrm{AEA} = \ln[\beta_{\mathrm{abs}}(405\ \ \mathrm{nm})/\beta_{\mathrm{abs}}(870\ \ \mathrm{nm})]/\ln[870/405] \tag{B1}$$

where β_{abs}(405 nm) and β_{abs}(870 nm) are the absorption coefficients for 405 nm and 870 nm, respectively. The experiment measured AEA using the PIN instrument. Diel averages of AEA (405–870 nm) are shown in Figure B4. June, July, and August observations demonstrated diurnal cycles of AEA.

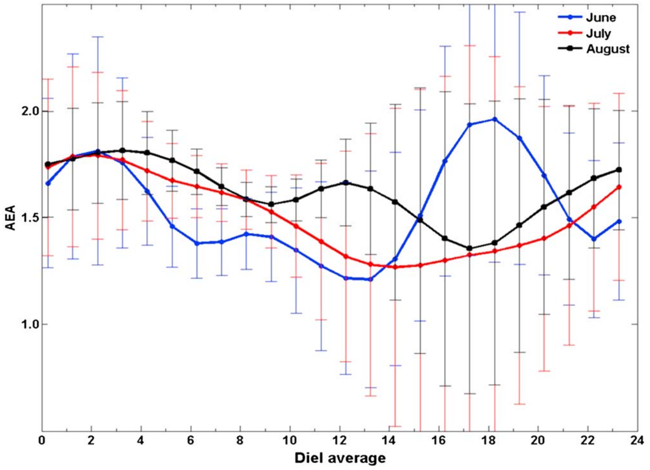

Figure B4. Diel average of ground-level AEA was measured at 405–870 nm for the months of June, July, and August, 2012. Uncertainty on AEA was determined by assuming 5% of relative uncertainty in photoacoustic measurements, and the propagation error equation was associated with aerosol light absorption observations.

During June, AEA varied from 1.21 to 1.96. Local minima were reached during the morning rush hour, which can be attributed to local dominance of vehicular emissions, and at noon when black carbon concentration is diminished by the expansion of the boundary layer. However, large values of AEA during June afternoons may be related with the presence of coarse particles. July had similar ranges to June with AEA from 1.26 to 1.79. The July curve shows a decreasing trend from 2 A.M. to 2 P.M. August AEA varied from 1.35 to 1.81 and has typical values for fire conditions.

Following the same procedure as explained in Appendix A near equation (A8), the AEA uncertainty equation that relates absorption coefficient measurements and absorption coefficients uncertainties at 405 and 870 nm is given by the following equation:

$$\Delta\mathrm{AEA} = \pm \frac{\sqrt{\left(\frac{\Delta\beta(\lambda_1)_{\mathrm{abs}}}{\beta(\lambda_1)_{\mathrm{abs}}}\right)^2 + \left(\frac{\Delta\beta(\lambda_2)_{\mathrm{abs}}}{\beta(\lambda_2)_{\mathrm{abs}}}\right)^2}}{\ln(870/405)}. \tag{B2}$$

The ranges for AEA uncertainties were from 0.17 to 0.67 (June), from 0.13 to 0.98 (July), and from 0.08 to 0.69 (August). These represent from 6 to 54% of variability of the data and explain why the error bars in Figure B4 are relatively large for some measurements.

Acknowledgment
This work was supported by NASA EPSCoR under cooperative agreement NNX10AR89A.

References

Andrews, E., P. J. Sheridan, J. A. Ogren, and R. Ferrare (2004), In situ aerosol profiles over the southern Great Plains cloud and radiation test bed site: 1. Aerosol optical properties, *J. Geophys. Res.*, *109*, D06208, doi:10.1029/2003JD004025.

Andrews, E., P. J. Sheridan, and J. A. Ogren (2011), Seasonal differences in the vertical profiles of aerosol optical properties over rural Oklahoma, *Atmos. Chem. Phys.*, *11*(20), 10,661–10,676, doi:10.5194/acp-11-10661-2011.

Ångström, A. (1929), On the atmosphere transmission of sun radiation and on dust in the air, *Geogr. Ann.*, *12*, 130–159.

Arnott, W. P., H. Moosmüller, C. F. Rogers, T. Jin, and R. Bruch (1999), Photoacoustic spectrometer for measuring light absorption by aerosol: Instrument description, *Atmos. Environ.*, *33*(17), 2845–2852, doi:10.1016/S1352-2310(98)00361-6.

Arnott, W. P., H. Moosmüller, and J. W. Walker (2000), Nitrogen dioxide and kerosene-flame soot calibration of photoacoustic instruments for measurement of light absorption by aerosols, *Rev. Sci. Instrum.*, *71*(12), 4545, doi:10.1063/1.1322585.

Atkinson, D. B., P. Massoli, N. T. O'Neill, P. K. Quinn, S. D. Brooks, and B. Lefer (2010), Comparison of in situ and columnar aerosol spectral measurements during TexAQS-GoMACCS 2006: Testing parameterizations for estimating aerosol fine mode properties, *Atmos. Chem. Phys.*, *10*, 51–61.

Bergin, M. H., S. E. Schwartz, R. N. Halthore, J. A. Ogren, and D. L. Hlavka (2000), Comparison of aerosol optical depth inferred from surface measurements with that determined by Sun photometry for cloud-free conditions at a continental US site, *J. Geophys. Res.*, *105*, 6807–6816, doi:10.1029/1999JD900454.

Chew, B. N., J. R. Campbell, S. V. Salinas, C. W. Chang, J. S. Reid, E. J. Welton, B. N. Holben, and S. C. Liew (2013), Aerosol particle vertical distributions and optical properties over Singapore, *Atmos. Environ.*, *79*, 599–613, doi:10.1016/j.atmosenv.2013.06.026.

Chylek, P., and J. Wong (1995), Effect of absorbing aerosols on global radiation budget, *Geophys. Res. Lett.*, *22*, 929–931, doi:10.1029/95GL00800.

Corbin, K. C., S. M. Kreidenweis, and T. H. Vonder Haar (2002), Comparison of aerosol properties derived from Sun photometer data and ground-based chemical measurements, *Geophys. Res. Lett.*, *29*(10), 1363, doi:10.1029/2001GL014105.

Draxler, R. R., and G. D. Rolph (2013), HYSPLIT (HYbrid Single-Particle Lagrangian Integrated Trajectory) Model, NOAA Air Resour. Lab., Silver Spring, Md. [Access via NOAA ARL READY Web site http://ready.arl.noaa.gov/HYSPLIT.php.]

Dubovik, O., and M. D. King (2000), A flexible inversion algorithm for retrieval of aerosol optical properties from sun and sky radiance measurements, *J. Geophys. Res.*, *105*, 20,673–20,696, doi:10.1029/2000JD900282.

Dubovik, O., A. Smirnov, B. N. Holben, M. D. King, Y. J. Kaufman, T. F. Eck, and I. Slutsker (2000), Accuracy assessments of aerosol optical properties retrieved from aerosol robotic network (AERONET) Sun and sky radiance measurements, *J. Geophys. Res.*, *105*, 9791–9806, doi:10.1029/2000JD900040.

Dubovik, O., B. N. Holben, T. Lapyonok, A. Sinyuk, M. I. Mishchenko, P. Yang, and I. Slutsker (2002), Non-spherical aerosol retrieval method employing light scattering by spheroids, *Geophys. Res. Lett.*, *29*(10), 1415, doi:10.1029/2001GL014506.

Dubovik, O., et al. (2006), Application of spheroid models to account for aerosol particle nonsphericity in remote sensing of desert dust, *J. Geophys. Res.*, *111*, D11208, doi:10.1029/2005JD006619.

Eck, T. F. (2010), AERONET—An internationally federated network, aerosol observability workshop—Monterey, April 28. [Available at http://icap.atmos.und.edu/ObservabilityMeeting/MeetingPDFs/Day-2/8_AERONET-Eck.pdf.]

Eck, T. F., B. N. Holben, J. S. Reid, O. Dubovik, A. Smirnov, N. T. O'Neill, I. Slutsker, and S. Kinne (1999), Wavelength dependence of the optical depth of biomass burning, urban, and desert dust aerosols, *J. Geophys. Res.*, *104*, 31,333–31,349, doi:10.1029/1999JD900923.

Eck, T. F., B. N. Holben, J. S. Reid, N. T. O'Neill, J. S. Schafer, O. Dubovik, A. Smirnov, M. A. Yamasoe, and P. Artaxo (2003), High aerosol optical depth biomass burning events: A comparison of optical properties for different source regions, *Geophys. Res. Lett.*, *30*(20), 2035, doi:10.1029/2003GL017861.

Fast, J. D., et al. (2012), Transport and mixing patterns over Central California during the carbonaceous aerosol and radiative effects study (CARES), *Atmos. Chem. Phys.*, *12*, 1759–1783, doi:10.5194/acp-12-1759-2012.

Finlayson-Pitts, B. J., and J. N. Pitts Jr. (1997), Tropospheric air pollution: Ozone, airborne toxics, polycyclic aromatic hydrocarbons, and particles, *Science*, *276*(5315), 1045–1052, doi:10.1126/science.276.5315.1045.

Goldstein, A. H., C. D. Koven, C. L. Heald, and I. Y. Fung (2009), Biogenic carbon and anthropogenic pollutants combine to form a cooling haze over the southeastern United States, *Proc. Natl. Acad. Sci. U.S.A.*, *106*(22), 8835–8840, doi:10.1073/pnas.0904128106.

Griffin, R. J., D. R. Crocker, R. C. Flagan, and J. H. Seinfeld (1999a), Organic aerosol formation from the oxidation of biogenic hydrocarbons, *J. Geophys. Res.*, *104*, 3555–3567, doi:10.1029/1998JD100049.

Griffin, R. J., D. R. Crocker, J. H. Seinfeld, and D. Dabdub (1999b), Estimate of global atmospheric organic aerosols from oxidation of biogenic hydrocarbons, *Geophys. Res. Lett.*, *26*, 2721–2724, doi:10.1029/1999GL900476.

Gyawali, M., W. P. Arnott, K. Lewis, and H. Moosmüller (2009), In-situ aerosol optics in Reno, NV, USA during and after the summer 2008 California wildfires and the influence of absorbing and non-absorbing organic coatings on spectral light absorption, *Atmos. Chem. Phys.*, *9*(20), 8007–8015, doi:10.5194/acp-9-8007-2009.

Gyawali, M., et al. (2013), Evolution of multispectral aerosol optical properties in a biogenically-influenced urban environment during the CARES campaign, *Atmos. Chem. Phys. Discuss.*, *13*, 7113–7150, doi:10.5194/acpd-13-7113-2013.

Hoff, R. M., and S. A. Christopher (2009), Remote sensing of particulate pollution from space: Have we reached the promised land?, *J. Air Waste Manage. Assoc.*, *59*(6), 645–675.

Hoffmann, T., J. R. Odum, F. Bowman, D. Collins, D. Klockow, R. C. Flagan, and J. H. Seinfeld (1997), Formation of organic aerosols from the oxidation of biogenic hydrocarbons, *J. Atmos. Chem.*, *26*(2), 189–222, doi:10.1023/A:1005734301837.

Holben, B. N., A. Setzer, T. F. Eck, A. Pereira, and I. Slutsker (1996), Effect of dry-season biomass burning on Amazon Basin aerosol concentrations and optical properties, 1992–1994, *J. Geophys. Res.*, *101*, 19,465–19,481, doi:10.1029/96JD01114.

Holben, B. N., et al. (1998), AERONET—A federated instrument network and data archive for aerosol characterization, *Remote Sens. Environ.*, *66*(1), 1–16, doi:10.1016/S0034-4257(98)00031-5.

Kaskaoutis, D. G., H. D. Kambezidis, N. Hatzianastassiou, P. G. Kosmopoulos, and K. V. S. Badarinath (2007), Aerosol climatology: Dependence of the Ångström exponent on wavelength over four AERONET sites, *Atmos. Chem. Phys. Discuss.*, *7*(3), 7347–7397, doi:10.5194/acpd-7-7347-2007.

Kassianov, E. I., M. S. Pekour, and J. C. Barnard (2012), Aerosols in Central California: Unexpectedly large contribution of coarse mode to aerosol radiative forcing, *Geophys. Res. Lett.*, *39,* L20806, doi:10.1029/2012GL053469.

Kim, D., M. Chin, H. Yu, T. F. Eck, A. Sinyuk, A. Smirnov, and B. Holben (2011), Dust optical properties over North Africa and Arabian Peninsula derived from the AERONET data set, *Atmos. Chem. Phys.*, *11*, 10,733–10,741, doi:10.5194/acp-11-10733-2011.

Kingsmill, D. (2000), Diurnally driven summertime winds in the lee of the Sierra: The Washoe Zephyr, Ninth conference on mountain meteorology, Session 6, Lee-side phenomena: Wakes and Downslope Winds, Wednesday, 9 August, 1:30 PM-3:59 PM. [Available at https://ams.confex.com/ams/AugAspen/techprogram/paper_15742.htm.]

Lensky, I. M., and D. Rosenfeld (1998), Satellite–based insights into precipitation formation processes in continental and maritime convective clouds, *Bull. Am. Meteorol. Soc.*, *79*, 2457–2476, doi:10.1175/1520-0477(1998)079<2457:SBIIPF>2.0.CO;2.

Lewis, K., W. P. Arnott, H. Moosmüller, and C. E. Wold (2008), Strong spectral variation of biomass smoke light absorption and single scattering albedo observed with a novel dual-wavelength photoacoustic instrument, *J. Geophys. Res.*, *113*, D16203, doi:10.1029/2007JD009699.

Lewis, K., et al. (2009), Reduction in biomass burning aerosol light absorption upon humidification: Roles of inorganically-induced hygroscopicity, particle collapse, and photoacoustic heat and mass transfer, *Atmos. Chem. Phys.*, *9*, 8949–8966, doi:10.5194/acp-9-8949-2009.

Moosmüller, H., and R. K. Chakrabarty (2011), Technical note: Simple analytical relationships between Ångström coefficients of aerosol extinction, scattering, absorption, and single scattering albedo, *Atmos. Chem. Phys.*, *11*, 10,677–10,680.

Paredes-Miranda, G., W. P. Arnott, J. L. Jimenez, A. C. Aiken, J. S. Gaffney, and N. A. Marley (2009), Primary and secondary contributions to aerosol light scattering and absorption in Mexico City during the MILAGRO 2006 campaign, *Atmos. Chem. Phys.*, *9*(11), 3721–3730, doi:10.5194/acp-9-3721-2009.

Pope, C. A., and D. W. Dockery (2006), Health effects of fine particulate air pollution: Lines that connect, *J. Air Waste Manage. Assoc.*, *56*(6), 709–742.

Prats, N., V. E. Cachorro, A. Berjon, C. Toledano, and A. M. De Frutos (2011), Column-integrated aerosol microphysical properties from AERONET Sun photometer over southwestern Spain, *Atmos. Chem. Phys.*, *11*(24), 12,535–12,574, doi:10.5194/acp-11-12535-2011.

Remer, L. A., Y. J. Kaufman, B. N. Holben, A. M. Thompson, and D. McNamara (1998), Biomass burning aerosol size distribution and modeled optical properties, *J. Geophys. Res.*, *103*, 31,879–31,891, doi:10.1029/98JD00271.

Remer, L. A., et al. (2005), The MODIS aerosol algorithm, products, and validation, *J. Atmos. Sci.*, *62*(4), 947–973, doi:10.1175/JAS3385.1.

Rolph, G. D. (2013), Real-time Environmental Applications and Display sYstem (READY), NOAA Air Resour. Lab., Silver Spring, Md. [Available at http://ready.arl.noaa.gov.]

Rosenfeld, D., W. L. Woodley, D. Axisa, E. Freud, J. Hudson, and A. Givati (2008), Aircraft measurements of the impacts of pollution aerosols on clouds and precipitation over the Sierra Nevada, *J. Geophys. Res.*, *113*, D15203, doi:10.1029/2007JD009544.

Rozwadowska, A. (2007), Influence of aerosol vertical profile variability on retrievals of aerosol optical thickness from NOAA AVHRR measurements in the Baltic region, *Oceanology*, *49*(2), 165–184.

Savitzky, A., and M. J. E. Golay (1964), Smoothing and differentiation of data by simplified least squares procedures, *Anal. Chem.*, *36*(8), 1627–1639, doi:10.1021/ac60214a047.

Schuster, G., O. Dubovik, and B. Holben (2006), Ångström exponent and bimodal aerosol size distributions, *J. Geophys. Res.*, *111*, D07207, doi:10.1029/2005JD006328.

Sheridan, P. J., A. Jefferson, and J. A. Ogren (2002), Spatial variability of submicrometer aerosol radiative properties over the Indian ocean during INDOEX, *J. Geophys. Res.*, *107*(D19), 8011, doi:10.1029/2000JD000166.

Sheridan, P. J., E. Andrews, J. A. Ogren, J. L. Tackett, and D. M. Winker (2012), Vertical profiles of aerosol optical properties over central Illinois and comparison with surface and satellite measurements, *Atmos. Chem. Phys.*, *12*(23), 11,695–11,721, doi:10.5194/acp-12-11695-2012.

Shilling, J. E., et al. (2013), Enhanced SOA formation from mixed anthropogenic and biogenic emissions during the CARES campaign, *Atmos. Chem. Phys.*, *13*, 2091–2113, doi:10.5194/acp-13-2091-2013.

Solomon, S., D. Qin, M. Manning, Z. Chen, M. Marquies, K. B. Averyt, M. Tignor, and H. L. Miller (Eds.) (2007), *IPCC-Report 2007*, chap. 2.4, Cambridge Univ. Press, Cambridge, U. K., and New York.

Stocker, T. F., et al. (Eds.) (2013), *Climate Change 2013: The Physical Science Basis. Contribution of Working Group I to the Fifth Assessment Report of the Intergovernmental Panel on Climate Change*, 1535 pp., Cambridge Univ. Press, Cambridge, U. K., and New York, doi:10.1017/CBO9781107415324.

Twomey, S. (1977), The influence of pollution on the shortwave albedo of clouds, *J. Atmos. Sci.*, *34*, 1149–1152, doi:10.1175/1520-0469(1977)034<1149:TIOPOT>2.0.CO;2.

Watson, J. G. (2002), 2002 Critical review—Visibility: Science and regulation, *J. Air Waste Manage. Assoc.*, *52*(6), 626–713.

Zaveri, R. A., et al. (2012), Overview of the 2010 Carbonaceous Aerosols and Radiative Effects Study (CARES), *Atmos. Chem. Phys.*, *12*, 7647–7687, doi:10.5194/acp-12-7647-2012.

Zhong, S., J. Li, C. B. Clements, S. De Wekker, and B. Xindi (2008), Forcing mechanisms for Washoe Zephyr—A daytime downslope wind system in the lee of the Sierra Nevada, *J. Appl. Meteorol. Climatol.*, *47*, 339–350, doi:10.1175/2007JAMC1576.1.